Dynamical cluster-decay model using various formulations of a proximity potential for compact non-coplanar nuclei: Application to the ^{64}Ni + ^{100}Mo reaction

Manie Bansal, Sahila Chopra, and Raj K. Gupta
Department of Physics, Panjab University, Chandigarh 160014, India

Raj Kumar and Manoj K. Sharma
School of Physics and Materials Science, Thapar University, Patiala 147004, India

(Received 24 July 2012; published 12 September 2012)

The dynamical cluster-decay model (DCM), using the well-known pocket formula of Blocki *et al*. [Ann. Phys. (NY) **105**, 427 (1977)] for nuclear proximity potential, is extended to the use of various other nuclear proximity potentials with effects of deformations included up to hexadecapole (β_4) and "compact" orientations taken for both coplanar ($\Phi = 0$) and non-coplanar ($\Phi \neq 0$) configurations of nuclei for the first time. The other nuclear proximity potentials used are those derived from the Skyrme-energy-density-formalism-based semiclassical extended Thomas Fermi method under frozen density approximation for a compound nucleus, using SIII and GSkI Skyrme forces. This is in addition to extending the Blocki *et al*. interaction to "compact" and non-coplanar nuclei. Application of the method is made to the study of the decay of the hot and rotating compound nucleus ^{164}Yb*, formed in the heavy-ion reaction ^{64}Ni + ^{100}Mo at both below- and above-barrier energies. For the best fitted measured evaporation residue cross-sections, consisting of x neutrons (x = 1–4), the interesting result of including the Φ degree of freedom is to increase the neck-length parameter of the model which results in the decrease of reaction time as well as the "barrier-lowering" parameter responsible for fusion hindrance effect. In other words, the fusion hindrance effect, a built-in property of DCM, though different for different nuclear interactions, reduces for the non-coplanar nuclei, and this reduction is more at higher center-of-mass energies. In the case of fusion-fission, only the CASCADE cross sections are available, which, when fitted simultaneously to another neck-length parameter, result in different components of a fusion-fission cross section for different nuclear interactions, including also the possibility of quasifission at the highest energy and the symmetric fission alone, that is, no intermediate-mass fragments, etc. The non-coplanar degree of freedom also plays an important role in changing the constituents of the fusion-fission cross section significantly, say, from intermediate and heavy-mass fragments plus the symmetric fission to simply the intermediate-mass fragments plus near-symmetric fission. This situation calls for the data for fusion-fission cross sections.

DOI: 10.1103/PhysRevC.86.034604 PACS number(s): 25.60.Pj, 25.70.Gh, 25.70.Jj, 27.70.+q

I. INTRODUCTION

^{64}Ni + ^{100}Mo → ^{164}Yb* is a very well-studied reaction, both experimentally [1–3] and theoretically [4–7]. This is a pure compound nucleus (CN) reaction because only the fusion-evaporation residue (ER) cross section $\sigma_{\rm ER}$, owing to the emission of light particles (LPs), is measured down to extreme sub-barrier energies, but no fusion-fission (ff) cross-section $\sigma_{\rm ff}$ could be measured at the near- and/or above-barrier energies in spite of an estimate from the CASCADE code being available at the highest two to three energies [1]. The fission channel can occur owing to any one or all of the CN decay processes of intermediate-mass fragments (IMFs), heavy-mass fragments (HMF), and the near-symmetric and symmetric fission (nSF and SF) fragments, that is, $\sigma_{\rm ff} = \sigma_{\rm IMF} + \sigma_{\rm HMF} + \sigma_{\rm nSF} + \sigma_{\rm SF}$, where one or all the terms contribute. Then, there could be the (also not observed for this reaction) non-CN decay to the quasifission (qf) or deep-inelastic process, where the incoming channel keeps its identity, such that the total fusion cross section $\sigma_{\rm fus} = \sigma_{\rm ER} + \sigma_{\rm ff} + \sigma_{\rm qf}$. The important point is that different decay modes are dominant in different nuclear reactions. The competing qf process for superheavy compound systems is referred [8] to as the "capture" process; that is, $\sigma_{\rm qf} = \sigma_{\rm cap}$.

Jiang *et al*. [1] have measured the excitation functions for ^{64}Ni + ^{100}Mo reaction for the incident center-of-mass (c.m.) energy range $E_{\rm c.m.}$ = 119.5 to 158.8 MeV, where the cross-section consists of $\sigma_{\rm ER}$ for the below- and above-barrier energies and the CASCADE estimates of $\sigma_{\rm ff}$ at above-barrier energies (barrier lies around $E_{\rm c.m.} \approx 140$ MeV for ^{64}Ni + ^{100}Mo). At sub-barrier energies, in an earlier experiment, Halbert *et al*. [3] obtained the spin distributions for the entry states of each exit channel. (The entry state of an exit channel or decay product is the state from which it goes to the ground state via γ-ray cascade after all LPs emission have taken place.) The LP-evaporation channels in this work are mainly the $2n$, $3n$, $4n$, and $\alpha 2n$, whose angular momentum ℓ dependencies, that is, $\sigma_{xn}(\ell)$, $x = 2, 3, \ldots$, are measured [3]. At and above barrier energies, in a later experiment, Ackermann *et al*. [2] measured the spin distributions (the ℓ dependence of the cross section) and observed the influence of $\sigma_{\rm ff}$ at above-barrier energies as a long tail in the high-spin region of the measured spin distribution.

Theoretically, the above-given data for ^{64}Ni + ^{100}Mo → ^{164}Yb* have been analyzed on many models, such as the coupled-channel calculations (ccc) [1,4], the Wong and (ℓ-summed) extended-Wong model [5,6], and the dynamical

cluster-decay model (DCM) [7]. In this paper, we extend the work of Ref. [7] on DCM, which is based on the nuclear proximity potential of Blocki *et al*. [9], where the effects of quadrupole to hexadecapole deformations (β_{2i}, β_{3i}, β_{4i}) and "optimum" orientations ($\theta_i^{\rm opt}$, $i = 1, 2$) for two nuclei in the same plane (coplanar nuclei) are included [10]. However, $\theta_i^{\rm opt}$ are given for quadrupole deformation β_{2i} alone (i.e., $\beta_{3i} = 0$, $\beta_{4i} = 0$), and for deformations up to β_{4i}, one must use the "compact" orientations θ_{ci} [11], which is done here in this paper. The difference between the "compact" and "optimum" configurations can be significantly large ($\sim 20^\circ$) [11]. We further notice that, for the Blocki *et al*. potential used in [7], the total decay or fusion cross section $\sigma_{\rm fus}$ for ^{164}Yb* is found to constitute the fusion-evaporation cross section $\sigma_{\rm ER}$ (owing to LPs consisting of x neutrons, $x = 1$–4) and the ff cross section $\sigma_{\rm ff}$ consisting of IMF, HMF, nSF, and SF. Because the ff of ^{64}Ni + ^{100}Mo is not yet observed, it will be interesting to see the predictions of DCM for use of other nuclear potentials, such as the nuclear proximity potential derived from Skyrme energy density formalism (SEDF) in semiclassical extended Thomas Fermi (ETF) approach [12]. This gives a variety of nuclear proximity potentials for different Skyrme nucleus-nucleus interactions (more commonly known as Skyrme forces) and is found [13] to give more realistic barriers in frozen density approximation of adding the densities for the CN, as compared to the sudden approximation. We do this here in this paper for two Skyrme forces SIII and GSkI, and find that the calculated $\sigma_{\rm ff}$ show important differences with the Blocki *et al*. interaction used in Ref. [7].

Another point of interest in this study is the inclusion of non-coplanar degree of freedom, the azimuthal angle Φ, in our use of the DCM for non-coplanar nuclei [6]. As already noted in Ref. [5], this would necessitate refitting of the only parameter of the model, the neck-length parameter ΔR, which could have at least two consequences: First, the constituents of ff process (components of $\sigma_{\rm ff}$) could be different for non-coplanar ($\Phi \neq 0^\circ$) nuclei, as compared to the case of coplanar nuclei ($\Phi = 0^\circ$) in Ref. [7]. Second, different ΔR means different "barrier lowering" parameter ΔV_B. Because barrier lowering at sub-barrier energies is a built-in property of DCM [6,7], it would be interesting to see if non-coplanar degree of freedom Φ provides a rescue to the "fusion hindrance" problem in ccc calculations [4] for ^{64}Ni + ^{100}Mo reaction, or else, how does the magnitude of ΔV_B vary for different proximity potentials used here. Similarly, at above-barrier energies, the non-coplanarity could influence the contribution of the qf component in fission cross section [6].

The paper is organized as follows: A brief account of the DCM for a hot and rotating CN is given in Sec. II. The nuclei are considered deformed with quadrupole, octupole, and hexadecapole deformations (β_{2i}, β_{3i}, β_{4i}) taken from Möller *et al*. [14] and "compact" orientation (θ_{ci}, Φ_c) calculated as per the method described in Ref. [11] for both the coplanar ($\Phi_c = 0^\circ$) and non-coplanar ($\Phi_c \neq 0^\circ$) configurations. The nuclear proximity potential is either from the pocket formula of Blocki *et al*. [9] or the one derived from SEDF-based semiclassical ETF method for different Skyrme forces [12]. Application of DCM to ^{64}Ni + ^{100}Mo $\rightarrow$ ^{164}Yb* reaction is made in Sec. III, with at least the following three interests in view: (i) to include the "compact" orientations for both the coplanar and non-coplanar configurations, (ii) to study the effect of different nuclear interactions on the ff cross section, and (iii) to see the effect of Skyrme forces on "barrier modification" problem at sub-barrier energies, and the contribution of the qf in fission cross section at above-barrier energies. The experimental data on fusion-evaporation cross section $\sigma_{\rm ER}$ and CASCADE calculations for ff cross-section $\sigma_{\rm ff}$ are taken from Ref. [1], and the information on evaporation channels and the channel cross sections are from Refs. [2,3]. Finally, a brief summary and discussion of our results is added in Sec. IV.

II. THE DYNAMICAL CLUSTER-DECAY MODEL FOR A HOT AND ROTATING COMPOUND NUCLEUS, USING DIFFERENT NUCLEAR PROXIMITY POTENTIALS

The DCM of Gupta and collaborators [6,7,15–19] is worked out in terms of the collective coordinates of mass (and charge) asymmetries $\eta = \frac{A_1 - A_2}{A_1 + A_2}$ ($\eta_Z = \frac{Z_1 - Z_2}{Z_1 + Z_2}$; 1 and 2 stand, respectively, for heavy and light fragments) and the relative separation R ($\geqslant R_1 + R_2$), to which is added the multipole deformations $\beta_{\lambda i}$ ($\lambda = 2, 3, 4$), orientations θ_i ($i = 1, 2$) of two nuclei or fragments, and the azimuthal angle Φ between their principal planes. Note that the deformations $\beta_{\lambda i}$ are different for different mass fragments; that is, $\beta_{\lambda i}$ are different for different mass asymmetries η, taken to be the same during the fusion and decay processes. However, the fusion probability in DCM is taken to be unity (see below), and hence for fusion only the incoming channel plays the role.

In terms of the above coordinates, for ℓ-partial waves, the CN decay or the fragment production cross section for each process is

$$\sigma(E_{\rm c.m.}, \theta_i, \Phi) = \sum_{\ell=0}^{\ell_{\max}} \sigma_\ell = \frac{\pi}{k^2} \sum_{\ell=0}^{\ell_{\max}} (2\ell + 1) P_0^\ell P_\ell, \qquad (1)$$

where $k = \sqrt{\frac{2\mu E_{\rm c.m.}}{\hbar^2}}$ with μ as the reduced mass. P_0^ℓ is the fragment preformation probability, referring to η motion, and P_ℓ is the transmission coefficient for each ℓ which describes the penetration of barrier $V_\eta(R, \ell)$, referring to R motion. Both P_0^ℓ and P_ℓ depend on $E_{\rm c.m.}$ (equivalently, temperature T, because the CN excitation energy $E^*_{\rm CN} = E_{\rm c.m.} + Q_{\rm in} = \frac{1}{10} A_{\rm CN} T^2 - T$; $Q_{\rm in}$ is the entrance channel Q value, and T is in MeV), $\beta_{\lambda i}$, θ_i of two nuclei, and Φ. The deformations of nuclei are kept fixed in R motion, and independent of temperature T, with the multipole deformations up to hexadecapole deformations (β_2-β_4) and orientations as "hot compact" θ_{ci} and Φ_c (referring to highest barrier and smallest interaction radius [11]). For T dependence of deformations, say, $\beta_2(T)$, we refer the reader to Refs. [20,21]. Equation (1) is used for all decay products (LPs, IMFs, HMFs, nSF, and SF) of a CN, which are all treated on equal footings as the dynamical collective mass motions of preformed clusters or fragments through the barrier $V_\eta(R, \ell)$.

The CN is considered to be formed with probability equal to one (an assumption more suitable for higher energies, but extended here also to lower energies) and, in general,

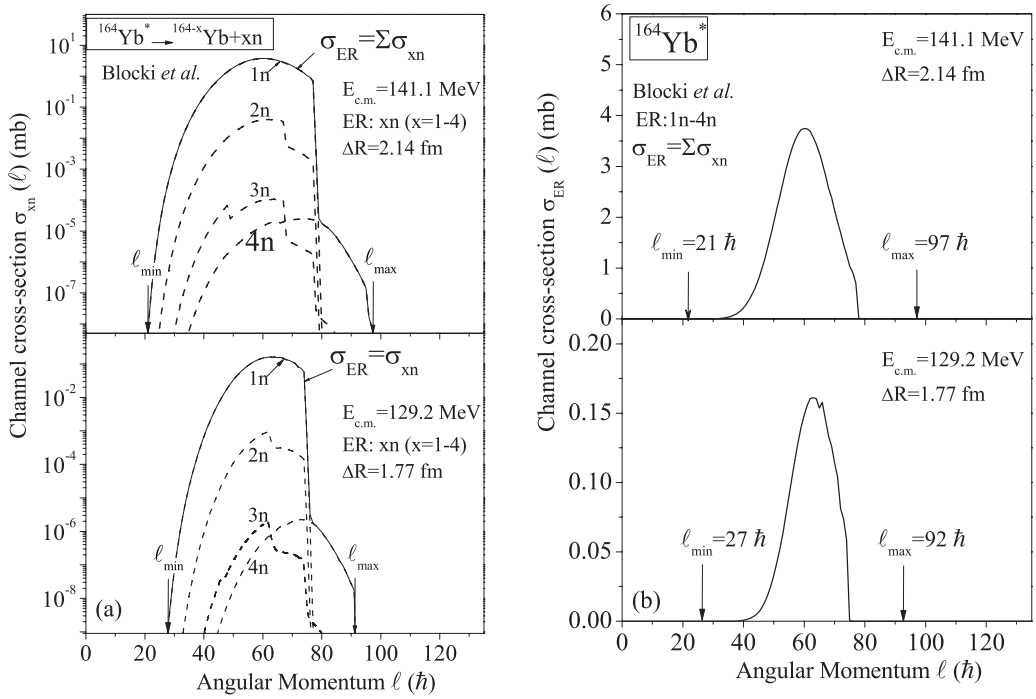

FIG. 1. (a) The channel cross section σ_{xn} ($x = 1$–4), and their sum $\sigma_{\rm ER}$, as a function of ℓ for LPs calculated at energies $E_{\rm c.m.} = 141.1$ and 129.2 MeV for the Blocki *et al.* potential ($\Phi \neq 0$ case), plotted on log scale. The $\ell_{\rm min}$ and $\ell_{\rm max}$ values are also marked. As for the $\Phi = 0$ case [7], the contribution of the $1n$ fragment is shown to be the largest, though contrary to the measurements of Halbert *et al.* [3]. (b) The total cross section $\sigma_{\rm ER}(\ell)$ at $E_{\rm c.m.} = 141.1$ and 129.2 MeV, plotted on a linear scale. Though the calculated distribution is similar to the measured one [3], a direct comparison is not possible because the calculated peak value for, say, $E_{\rm c.m.} = 141.1$ MeV is about two times higher than the measured value. Also, contrary to [3], the $4n$ contribution is four orders of magnitude smaller than the $1n$ contribution and occurs in a higher ℓ window. These points are discussed in detail in our earlier work [7] for the $\Phi = 0$ case, where the ℓ window is nearly the same for all xn emission and suggest the use of different ΔR values for different xn-emission data of Halbert *et al.* [3]. The same results follow for the SEDF-based interactions using different Skyrme forces.

independent of the incoming channel. The entrance channel effects in DCM enter via the maximum angular momentum $\ell_{\rm max}$ [22], which is fixed for the vanishing of the LPs cross section $\sigma_{\rm ER} \to 0$ (i.e., $\sigma_{\rm ER} > 10^{-9}$ mb) owing to $P_0 \to 0$ at $\ell = \ell_{\rm max}$, as is illustrated in Fig. 1 for an energy each below ($E_{\rm c.m.} = 129.2$ MeV) and above ($E_{\rm c.m.} = 141.1$ MeV) the barrier. Correspondingly, the minimum contributing ℓ value, the $\ell_{\rm min}$, is also fixed by the same process, owing to $P \to 0$ at $\ell \leqslant \ell_{\rm min}$. (For other details on LP channel cross section, etc., see the caption of Fig. 1). $\ell_{\rm max}$ could also be taken as a variable parameter [23]. For the qf process, the incoming channel keeps its identity, and hence in the case of qf, $P_0 = 1$ for all ℓ's [19].

The preformation probability $P_0^{\ell}(A_i)$ [$= |\psi(\eta(A_i))|^2 \sqrt{B}_{\eta\eta} \frac{2}{A_{\rm CN}}$] for each ℓ value is the solution of stationary Schrödinger equation in η, at a fixed $R = R_a$,

$$\left\{-\frac{\hbar^2}{2\sqrt{B}_{\eta\eta}}\frac{\partial}{\partial\eta}\frac{1}{\sqrt{B}_{\eta\eta}}\frac{\partial}{\partial\eta} + V_R(\eta, T)\right\}\psi_R^{(\nu)}(\eta) = E_R^{(\nu)}\psi_R^{(\nu)}(\eta), \tag{2}$$

where $R_a = R_1(\alpha_1, T) + R_2(\alpha_2, T) + \Delta R(\eta, T)$, with the radius vectors

$$R_i(\alpha_i, T) = R_{0i}(T)\left[1 + \sum_{\lambda}\beta_{\lambda i}Y_{\lambda}^{(0)}(\alpha_i)\right]. \tag{3}$$

$R_{0i}(T)$ are the T-dependent nuclear radii for the equivalent spherical nuclei [24],

$$R_{0i}(T) = \left[1.28A_i^{1/3} - 0.76 + 0.8A_i^{-1/3}\right](1 + 0.0007T^2). \tag{4}$$

In Eq. (2), $\nu = 0$, 1, 2, 3, ...refer to ground-state ($\nu = 0$) and excited-state solutions and, for a Boltzmann-like function, $|\psi|^2 = \sum_{\nu=0}^{\infty}|\psi^{(\nu)}|^2\exp(-E^{(\nu)}/T)$. R_a is (are) the first turning point(s) of the penetration path(s) used for calculating the penetrability P_ℓ, illustrated in Fig. 2 for two ℓ values at a fixed $E_{\rm c.m.}$ or T value.

The angle α_i in the above equations is that which the nuclear symmetry axis makes with the radius vector $R_i(\alpha_i)$, measured in the clockwise direction. This is to be distinguished from the orientation angle θ_i in Eq. (1) that the nuclear symmetry axis makes with the collision Z axis, measured in the anticlockwise direction (see Fig. 3). In the definition of R_a above, ΔR is the relative separation distance between two fragments/clusters A_i, as is also illustrated in Fig. 2. In the language of the two-center shell model (TCSM), used to determine shell effects δU [like in Eq. (6) below], ΔR is shown to assimilate the neck formation effects [25–27], and hence is referred to as the neck-length parameter. This is more true for fission fragments and not for neutron clusters as one of the fragments, but is similar to that used in both the scission-point [28] and

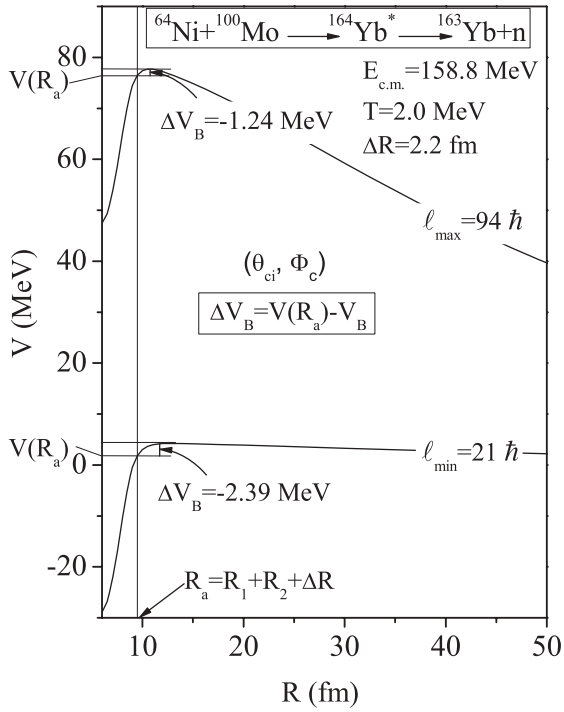

FIG. 2. The scattering potentials $V(R)$ for $^{64}\mathrm{Ni} + {}^{100}\mathrm{Mo} \rightarrow {}^{164}\mathrm{Yb}^{*} \rightarrow {}^{163}\mathrm{Yb} + n$, at two different ℓ values, calculated by using the Blocki *et al.* potential for compact orientations (θ_{ci}, Φ_c). The decay path, defined by $V(R_a, \ell)$ for each ℓ is shown to begin at $R_a = R_1 + R_2 + \Delta R$ for each ℓ value. The definition of "barrier lowering" $\Delta V_B = V(R_a) - V_B$ is also shown in this figure for both the $\ell_{\min}$ and the $\ell_{\max}$ values. Note, ΔV_B values reduce when going from $(\theta_i^{\mathrm{opt}}, \Phi{=}0)$ to (θ_{ci}, Φ_c) (compare with Fig. 1 of Ref. [7]).

saddle-point [23,29] statistical fission models for calculating the ER and fission cross sections. The parameter ΔR fixes the first turning point of barrier penetration, referring to the actually used barrier height $V(R_a, \ell)$, and consequently to the concept of "barrier lowering" $\Delta V_B(\ell)$ (defined below). It may be worth noting that the use of neck-length parameter, equivalently, "barrier modification," helps us to account for the fusion hindrance effect at sub-barrier energies, because the effective potential gets significantly modified. The choice of ΔR for the best fit to the data (here, ER) allows us to define

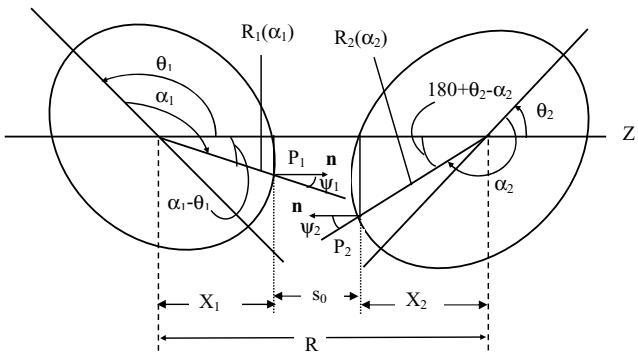

FIG. 3. Schematic configuration of any two axially symmetric deformed, oriented nuclei lying in the same plane ($\Phi = 0^{\circ}$).

the effective "barrier lowering" parameter $\Delta V_B(\ell)$ for each ℓ as the difference between the actually used barrier $V(R_a, \ell)$ and the top of the calculated barrier $V_B(\ell)$, as

$$\Delta V_B(\ell) = V(R_a, \ell) - V_B(\ell). \tag{5}$$

Note, ΔV_B is defined as a negative quantity, and hence the actually used barrier is effectively lowered, as shown in Fig. 2 for two ℓ values.

In Eq. (2), the mass parameters $B_{\eta\eta}$ are the smooth hydrodynamical masses [30], used for reasons of simplicity. Thus, the microscopic shell effects in masses $B_{\eta\eta}$ are not included here. A more realistic prescription would be to use the cranking masses, consistently calculated by using the underlying asymmetric two-center shell model (ATCSM) with BCS formalism as its basis (see, e.g., the $B_{\eta\eta}$ calculations in Refs. [31–33]).

The fragmentation potential $V_R(\eta, T)$ in Eq. (2) is defined as

$$\begin{aligned} V_R(\eta, T) &= -\sum_{i=1}^{2}[V_{\mathrm{LDM}}(A_i, Z_i, T)] + \sum_{i=1}^{2}[\delta U_i]\exp\left(-\frac{T^2}{T_0^2}\right) \\ &\quad + V_P(R, A_i, \beta_{\lambda i}, \theta_i, \Phi, T) + V_C(R, Z_i, \beta_{\lambda i}, \theta_i, \Phi, T) \\ &\quad + V_\ell(R, A_i, \beta_{\lambda i}, \theta_i, \Phi, T), \end{aligned} \tag{6}$$

where V_{LDM} is the T-dependent liquid drop energy of Davidson *et al.* [34], based on Seeger's semiempirical mass formula [35], and δU are the "empirical" shell corrections from Myers and Swiatecki [36], taken to go to zero exponentially with T. $T_0 =$ 1.5 MeV from the classical work of Jensen and Damgaard [37], which means that the shell-correction term becomes nearly zero for $T > 4$ MeV. Seeger's constants at $T = 0$ are refitted by one of us (R.K.G.) and collaborators [38–40] by defining the experimental binding energy B of a nucleus as $B = V_{\mathrm{LDM}}(T = 0) + \delta U$. This procedure takes care of the missing deformation effects in Ref. [36] to some extent and is applied to all nuclei. The T dependence in constants of V_{LDM} is then included as per Fig. 1 in Ref. [34]. A more realistic method for calculating the shell effects δU is to use, say, the deformed TCSM [41], but then we have to carry out a large numerical calculation, and thus lose the analyticity of Myers and Swiatecki's formula.

The terms V_C, V_ℓ, and V_P in Eq. (6), for coplanar ($\Phi = 0^{\circ}$) nuclei, are the T- and θ_i-dependent Coulomb and ℓ-dependent and nuclear proximity potentials, respectively, as

$$\begin{aligned} V_C &= \frac{Z_1 Z_2 e^2}{R} + 3Z_1 Z_2 e^2 \sum_{\lambda, i=1,2} \frac{R_i^{\lambda}(\alpha_i, T)}{(2\lambda+1)R^{\lambda+1}} \\ &\quad \times Y_\lambda^{(0)}(\theta_i)\left[\beta_{\lambda i} + \frac{4}{7}\beta_{\lambda i}^2 Y_\lambda^{(0)}(\theta_i)\right], \end{aligned} \tag{7}$$

$$V_\ell = \frac{\hbar^2 \ell(\ell+1)}{2I_S}, \tag{8}$$

with $I_S = \mu R^2 + \frac{2}{5}A_1 m R_1^2(\alpha_1, T) + \frac{2}{5}A_2 m R_2^2(\alpha_2, T)$, the sticking moment-of-inertia, and

$$V_P = 4\pi \bar{R}(T)\gamma b(T)\phi(D(T)), \tag{9}$$

where the nuclear surface thickness [24],

$$b(T) = 0.99(1 + 0.009T^2), \tag{10}$$

$\gamma = 0.9517[1 - 1.7826(\frac{N-Z}{A})^2]$ MeV fm^{-2} is the surface energy constant, and $\phi(D)$ is the universal function, which is independent of the shapes of nuclei or the geometry of nuclear system but depends on the dimensionless variable $D = s/b$, where $s(T)$ is the separation distance with a minimum value $s_0(T)$ (see Fig. 3). For the proximity potential of Blocki *et al.* [9],

$$\phi(D) = \begin{cases} -\frac{1}{2}(D - 2.54)^2 - 0.0852(D - 2.54)^3, \\ -3.437\exp\left(-\frac{D}{0.75}\right), \end{cases} \tag{11}$$

respectively, for $D(T) \leqslant 1.2511$ and $\geqslant 1.2511$, with the s_0 given as (see Fig. 3)

$$\begin{aligned} s_0 &= R - X_1 - X_2 \\ &= R - R_1(\alpha_1, T)\cos(\theta_1 - \alpha_1) - R_2(\alpha_2, T) \\ &\quad \times \cos(180 + \theta_2 - \alpha_2), \end{aligned} \tag{12}$$

minimized in α's. The minimization conditions, known as normal vector conditions, are

$$\begin{aligned} \tan(\theta_1 - \alpha_1) &= -\frac{R_1'(\alpha_1)}{R_1(\alpha_1)}, \\ \tan(180 + \theta_2 - \alpha_2) &= -\frac{R_2'(\alpha_2)}{R_2(\alpha_2)}, \end{aligned} \tag{13}$$

with the $R_i'(\alpha_i)$ being the first-order derivative of $R_i(\alpha_i)$ with respect to α_i.

Similarly, in the semiclassical ETF approach, based on SEDF, the universal function $\phi(D)$ of nuclear proximity potential in Eq. (9), for the Skyrme Hamiltonian density $H(\rho, \tau, \vec{J})$, is given as [12]

$$\begin{aligned} \phi(D) &= \frac{1}{2\gamma b}\int \{H(\rho, \tau, \vec{J}) - [H_1(\rho_1, \tau_1, \vec{J}_1) \\ &\quad + H_2(\rho_2, \tau_2, \vec{J}_2)]\}dz \\ &= \phi_P(D) + \phi_J(D), \end{aligned} \tag{14}$$

where

$$\phi_P(D) = \frac{1}{2\gamma b}\int \{H(\rho) - [H_1(\rho_1) + H_2(\rho_2)]\}dz,$$

$$\phi_J(D) = \frac{1}{2\gamma b}\int \{H(\vec{J}) - [H_1(\vec{J}_1) + H_2(\vec{J}_2)]\}dz,$$

for the composite system, under frozen density approximation, $\rho = \rho_1 + \rho_2$, $\tau = \tau(\rho) = \tau_1(\rho_1) + \tau_2(\rho_2)$, and $\vec{J} = \vec{J}(\rho) = \vec{J}_1(\rho_1) + \vec{J}_2(\rho_2)$. Note that in the ETF approach, though both the kinetic-energy density τ and spin-orbit density $\vec{J}$ are functions of the nuclear density ρ, the $\vec{J}$-dependent and $\vec{J}$-independent functions are written separately because the two behave differently [$\phi_P(D)$ is mainly attractive and $\phi_J(D)$ is mainly repulsive].

Then, following our earlier work [42], using the T-dependent two-parameter Fermi density (FD) distribution in slab approximation (required for proximity potential),

$$\begin{aligned} \rho_i(z_i) &= \rho_{0i}(T)\left[1 + \exp\left(\frac{z_i - R_{0i}(T)}{a_{0i}(T)}\right)\right]^{-1} \\ &\quad -\infty \leqslant z \leqslant \infty, \end{aligned} \tag{15}$$

with $z_2 = R - z_1$, and central density $\rho_{0i}(T) = \frac{3A_i}{4\pi R_{0i}^3(T)}[1 + \frac{\pi^2 a_{0i}^2(T)}{R_{0i}^2(T)}]^{-1}$; the universal functions $\phi_P(D)$ and $\phi_J(D)$ for use of the various Skyrme forces such as SII, SIII, SIV, SkM*, SLy4, SKa, MSK1, and SGII, etc., calculated for some 35 cases of colliding pairs of nuclei with CN mass up to $A = 294$, are parametrized [12] as

$$\phi_P(D) = \begin{cases} -\phi_P^0 \exp[-a(D - D_0)^{1.67}] & \text{for } D \geqslant D_0, \\ -\phi_P^0 + b(D - D_0)^2 & \text{for } D \leqslant D_0, \end{cases} \tag{16}$$

and

$$\phi_J(D) = \begin{cases} \phi_J^0 \exp[-cD^2] & \text{for } D \geqslant 0, \\ \phi_J^0 - dD - eD^2 - fD^3 - gD^4 & \text{for } D \leqslant 0, \end{cases} \tag{17}$$

with constants ϕ_P^0, D_0, a, and b of $\phi_P(D)$ and ϕ_J^0, c, d, e, f, and g of $\phi_J(D)$ for different Skyrme forces obtained as given in Table I of Ref. [12]. The constant ϕ_P^0 gives the maximum attraction of $\phi_P(D)$ at $D = D_0$ and ϕ_J^0 as the maximum repulsion of $\phi_J(D)$ at $D = 0$. The half-density radii $R_{0i}(T = 0)$ and surface-thickness parameters $a_{0i}(T = 0)$ in Eq. (15) are obtained [12] by fitting the experimental data to respective polynomials in nuclear mass range $A = 4$–238, to give

$$\begin{aligned} R_{0i}(T = 0) &= 0.9543 + 0.0994A_i - 9.8851 \times 10^{-4}A_i^2 \\ &\quad + 4.8399 \times 10^{-6}A_i^3 - 8.4366 \times 10^{-9}A_i^4, \end{aligned} \tag{18}$$

$$\begin{aligned} a_{0i}(T = 0) &= 0.3719 + 0.0086A_i - 1.1898 \times 10^{-4}A_i^2 \\ &\quad + 6.1678 \times 10^{-7}A_i^3 - 1.0721 \times 10^{-9}A_i^4. \end{aligned} \tag{19}$$

The temperature dependence in the above formulas are then introduced as in Ref. [43],

$$R_{0i}(T) = R_{0i}(T = 0)[1 + 0.0005T^2], \tag{20}$$

$$a_{0i}(T) = a_{0i}(T = 0)[1 + 0.01T^2]. \tag{21}$$

Note that the surface width b is also T dependent [Eq. (10)]. Apparently, $\phi(D)$ in Eq. (14) can be calculated "exactly" by solving the actual integrals or in terms of the parametrized polynomial functions of Eqs. (16) and (17). In the following, we solve the actual integrals in Eq. (14) for the Skyme forces SIII and GSkI. Note that SIII is an old force [44,45], and GSkI was given recently [46,47], made more appropriate for the isospin-rich nuclei, as is the case for the reaction studied here.

Next, $\bar{R}(T)$ in Eq. (9), the mean curvature radius, characterizing the points of closest approach s_0, for nuclei lying in the same plane ($\Phi = 0^\circ$), is

$$\frac{1}{\bar{R}^2} = \frac{1}{R_{11}R_{12}} + \frac{1}{R_{21}R_{22}} + \frac{1}{R_{11}R_{22}} + \frac{1}{R_{21}R_{12}}, \tag{22}$$

where R_{i1} and R_{i2} are the principal radii of curvatures at the points P_1 and P_2 in Fig. 3. For explicit expressions of R_{i1} and

TABLE I. Calculated fusion-evaporation cross sections $\sigma_{\rm ER}^{\rm Cal.}$ compared with the experimental $\sigma_{\rm ER}^{\rm Expt.}$ data of Ref. [1]. Also tabulated is the ff cross section $\sigma_{\rm ff}^{\rm Cal.}$, compared with the CASCADE data $\sigma_{\rm ff}^{\rm CASCADE}$ of Ref. [1]. The zeros in the last column are as quoted in Ref. [1]. In DCM calculations, the SF window for SIII and GSk1 ($\Phi = 0$) refers to $(A/2) \pm 17$. For Blocki *et al.* ($\Phi \neq 0$) ff consists of IMF and nSF, where IMF refers to $A_2 = 5$–14 and nSF to $A_2 = 61$–68 and its complimentary fragments. This is to be compared with Blocki *et al.* ($\Phi = 0$) where ff consists of IMF, HMF, and SF [7].

$E_{\rm c.m.}$ (MeV)	DCM $\sigma_{\rm ER}^{\rm Cal.}$ (mb) LPs ($1n$-$4n$)			Experimental $\sigma_{\rm ER}^{\rm Expt.}$ (mb) Ref. [1]	DCM $\sigma_{\rm ff}^{\rm Cal.}$ (mb) SF			Calculated $\sigma_{\rm ff}^{\rm CASCADE}$ (mb) Ref. [1]
	SIII ($\Phi = 0$)	GSkI ($\Phi = 0$)	Blocki ($\Phi \neq 0$)		SIII ($\Phi = 0$)	GSkI ($\Phi = 0$)	IMF + nSF Blocki ($\Phi \neq 0$)	
158.8	272.83	266.34	277.0154	264 ± 35	275.2	270.65	260.6	275
149.9	216.21	206.12	188.2143	210 ± 25	82.08	82.344	83.0	80
141.1	83.60	76.05	81.4355	80.0 ± 8.8	2.1508	2.2887	8.72	2
136.1	31.423	29.02	29.217	29.2 ± 3.0	0.193 11	0.0997	2.03	0
131.2	6.41	6.81	6.665	6.80 ± 0.71	5.46×10^{-3}	4.15×10^{-3}	0.4067	0
129.2	2.86	2.73	2.87	2.87 ± 0.30	3.24×10^{-4}	4.39×10^{-4}	0.1837	0
127.5	0.93	1.08	1.06	0.92 ± 0.10	2.11×10^{-5}	2.13×10^{-5}	0.0707	0
126.2	0.36	0.36	0.256	0.35 ± 0.04	2.21×10^{-6}	3.98×10^{-6}	0.011 56	0
125.0	0.107	0.103	0.1175	0.109 ± 0.012	5.18×10^{-7}	8.29×10^{-8}	3.106×10^{-3}	0
123.9	0.0274	0.0272	0.0278	0.0253 ± 0.0029	7.09×10^{-8}	7.22×10^{-9}	6.88×10^{-4}	0
123.3	0.0128	0.0145	0.0101	0.0132 ± 0.0014	2.29×10^{-8}	2.20×10^{-9}	1.84×10^{-4}	0
122.9	7.54×10^{-3}	7.46×10^{-3}	0.0058	$7.4 \pm 0.87 \times 10^{-3}$	1.31×10^{-8}	8.52×10^{-10}	5.63×10^{-5}	0
121.7	1.10×10^{-3}	1.31×10^{-3}	0.0018	$1.10 \pm 0.16 \times 10^{-3}$	5.34×10^{-10}	8.18×10^{-12}	1.41×10^{-5}	0
121.2	2.63×10^{-4}	2.62×10^{-4}	3.8×10^{-4}	$2.42 \pm 0.41 \times 10^{-4}$	2.50×10^{-11}	9.97×10^{-13}	3.05×10^{-6}	0
120.2	2.09×10^{-5}	1.75×10^{-5}	1.05×10^{-4}	$<2.0 \times 10^{-5}$	3.45×10^{-13}	1.76×10^{-14}	4.96×10^{-7}	0
119.5	4.78×10^{-6}	2.48×10^{-6}	1.83×10^{-5}	$<4.6 \times 10^{-6}$	6.56×10^{-14}	1.61×10^{-15}	8.54×10^{-8}	0

R_{i2} and other details on generalized proximity potential for coplanar nuclei, see Ref. [48].

Finally, for non-coplanar nuclei ($\Phi \neq 0^\circ$), we use the same formalism as for $\Phi = 0^\circ$ above, but by replacing the out-of-plane nucleus ($i = 1$ or 2) with the corresponding radius parameter $R_i(\alpha_i)$ with its projected radius parameter $R_i^P(\alpha_i)$ in both the Coulomb and the proximity potentials. For Coulomb potential, it enters via $R_i(\alpha_i)$ itself, and for the proximity potential it enters via the definitions of both the mean curvature radius $\bar{R}$ and the shortest distance s_0 [49]. The $R_i^P(\alpha_i)$ is determined by defining, for the out-of-plane nucleus, two principal planes $X'Z'$ and $Y'Z'$, respectively, with radius parameters $R_i(\alpha_i)$ and $R_j(\delta_j)$, such that their projections into the plane (XZ) of the other nucleus are (see Fig. 1 in Ref. [49])

$$R_i^P(\alpha_i) = R_i(\alpha_i)\cos\Phi \qquad i = 1 \text{ or } 2, \tag{23}$$

and

$$R_j^P(\delta_j) = R_j(\delta_j)\cos(\Phi - \delta_j) \quad j = i = 1 \text{ or } 2. \tag{24}$$

Then, maximizing $R_j(\delta_j)$ in angle δ_j, we get

$$\begin{aligned} R_i^P(\alpha_i) &= R_i^P(\alpha_i = 0^\circ) + R_i^P(\alpha_i \neq 0^\circ) \\ &= R_j^P\left(\delta_j^{\max}\right) + R_i(\alpha_i \neq 0^\circ)\cos\Phi, \end{aligned} \tag{25}$$

with $\delta_j^{\max}$ given by the condition (for fixed Φ),

$$\tan(\Phi - \delta_j) = -\frac{R_j'(\delta_j)}{R_j(\delta_j)}. \tag{26}$$

Thus, the Φ dependence of projected radius vector $R_i^P(\alpha_i)$ is also contained in maximized $R_j^P(\delta_j^{\max})$. For further details, see Ref. [49]. Then, for nuclear proximity potential, denoting by V_P^{12} the potential for the nucleus 1 to be out of plane and by V_P^{21} for the nucleus 2 to be out of plane, the effective nuclear proximity potential

$$V_P = \tfrac{1}{2}\left[V_P^{12} + V_P^{21}\right]. \tag{27}$$

Note that it is the first time that the semiclassical ETF approach based on SEDF is used in DCM for calculating the nuclear proximity potential.

The penetrability P_ℓ in Eq. (1) is the WKB integral between R_a and R_b, with R_b as the second turning point,

$$P_\ell = \exp\left[-\frac{2}{\hbar}\int_{R_a}^{R_b}\{2\mu[V_\ell(R,T) - Q_{\rm eff}]\}^{1/2}dR\right], \tag{28}$$

solved analytically, satisfying

$$V(R_a,\ell) = V(R_b,\ell) = Q_{\rm eff}(T, \ell = \ell_{\min}) = TKE(T). \tag{29}$$

This means that $V(R_a,\ell)$ acts like an effective Q value, $Q_{\rm eff}(T,\ell)$, given by the total kinetic energy TKE(T). As ℓ value increases, the $Q_{\rm eff}(T)$ [=TKE(T)] increases, and hence $V(R_a,\ell)$ increases. Thus, R_a acts like a parameter through $\Delta R(\eta, T)$, and we define that R_a is the same for all ℓ values, that is, $V(R_a) = Q_{\rm eff}(T, \ell = 0)$. This is required because we do not know how to add the ℓ effects in binding energies. It is

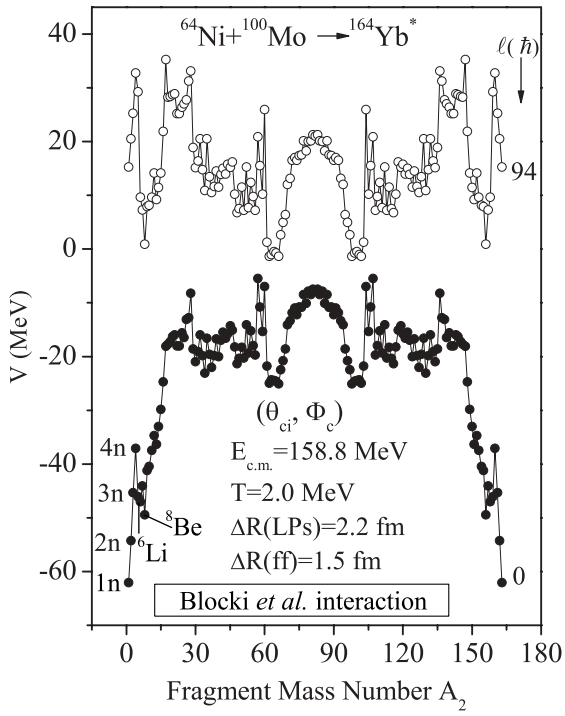

FIG. 4. The fragmentation potential $V(A_i)$ for the charge-favored fragments of the compound system ^{164}Yb* formed in the ^{64}Ni + ^{100}Mo reaction at a fixed temperature $T = 2.0$ MeV (equivalently, $E_{\rm c.m.} = 158.8$ MeV) and $\Delta R = 2.2$ fm for $A_2 = 1$–4 (and complimentary fragments) and 1.5 fm for all other heavier fragments, using compact orientations (θ_{ci}, Φ_c), for the Blocki *et al.* [9] interaction potential. Mass-1, -2, -3, and -4 fragments are taken to be $1n$ to $4n$.

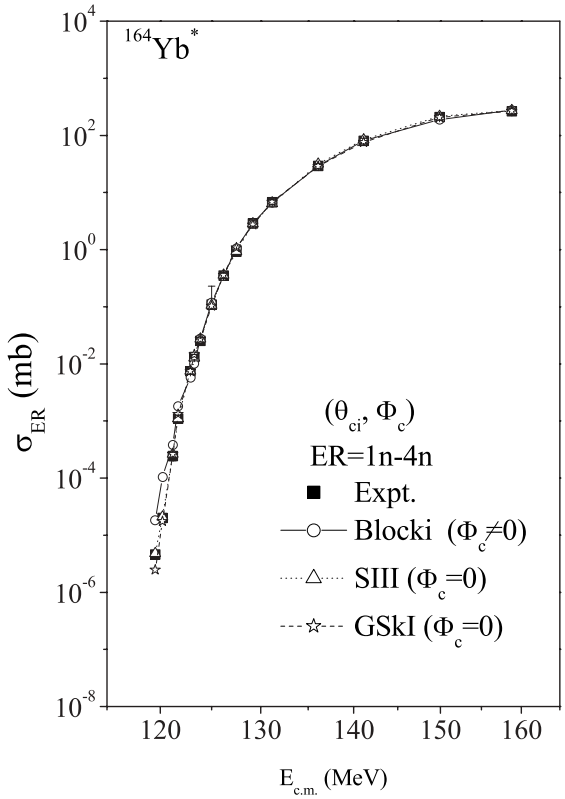

FIG. 5. Calculated fusion-evaporation excitation functions for ^{64}Ni + ^{100}Mo → ^{164}Yb* reaction using different nuclear interactions, compared with experimental data [1]. Φ is included for the case of Blocki *et al.*

relevant to remind the reader here also that the reduced mass μ in Eq. (28) is a rough approximation to the cranking mass B_{RR} in the R coordinate, whose average over η (i.e., $\bar{B}_{RR}$) goes to μ asymptotically (see, e.g., Fig. 2(a) in [50]). However, in this paper, we do not carry out the microscopic shell-model-based calculations.

III. CALCULATIONS AND RESULTS

A. Fusion-evaporation cross sections: Role of non-coplanarity and different nuclear interactions on fusion hindrance phenomenon

In this section, we look for the effects of adding a non-coplanar degree of freedom ($\Phi \neq 0$) and of using various nuclear interactions on the fusion hindrance phenomenon in the chosen ^{64}Ni + ^{100}Mo reaction.

Figure 4 illustrates the mass fragmentation potential $V(A_i)$, minimized in charge coordinate η_Z, for ^{164}Yb* using the Blocki *et al.* interaction potential at two ℓ values ($\ell = 0$ and $\ell_{\rm max}$), calculated for a fixed $T = 2.0$ MeV and $\Delta R = 2.2$ fm for LPs ($A_2 = 1$–4) and 1.5 fm for the remaining ff fragments ($A_2 = 5 - A/2$; discussed in next section). Here, $T = 2.0$ MeV corresponds to the highest center-of-mass energy $E_{\rm c.m.} = 158.8$ MeV and ΔR to the best fit of evaporation-residue (LPs) and CASCADE ff data in the ^{64}Ni + ^{100}Mo reaction [1]. Similar calculations are made for SEDF-based ETF method using Skyrme forces SIII and GSkI under frozen density approximation, resulting in similar $V(A_i)$ but with different ΔR values for an equally good fit to both ER and CASCADE fission data. In all cases, the energetically favored fragments for LPs were taken to be $1n$, $2n$, $3n$, and $4n$, even though $1n$ is not observed in experiments [3] but is known [7] to contribute maximum to ER cross section in DCM. Other minima of interest in Fig. 4 are the ^{6}Li and ^{8}Be minima because, in experiments at another above-barrier energy ($E_{\rm c.m.} = 141.7$ MeV) [3], one of the residues indicated is $\alpha 2n$, which may, in fact, be an IMF ^{6}Li, instead.

Table I and Fig. 5 show our calculated fusion-evaporation cross section $\sigma_{\rm ER}$ as a function of $E_{\rm c.m.}$ for the compound system ^{164}Yb*, using the Blocki *et al.* and Skyrme forces SIII and GSkI, compared with the experimental data [1]. Here, LPs consist of $1n$, $2n$, $3n$, and $4n$ and effects of deformations (β_2, β_3, β_4) and compact orientations of hot fusion (θ_{ci}, Φ_c) are included. $\Phi_c \neq 0$ for the Blocki *et al.* interaction but equal to zero for both the Skyrme forces, and the same ($\Phi_c = 0$) for the case of Blocki *et al.* interaction was studied earlier in Ref. [7], where the role of deformations was also shown to be important, and the contribution of mass-1 fragment ($1n$) to $\sigma_{\rm ER}$ was largest [this is also true for the present calculations of $\Phi_c \neq 0$, as is evident from Fig. 1(a)]. The only parameter of the model, used to fit the data, is the neck-length $\Delta R(T)$, obtained as shown in Fig. 6(a). The fitting of the data in Fig. 5 is rather very good in each case, with the $\Delta R(T)$ varying smoothly

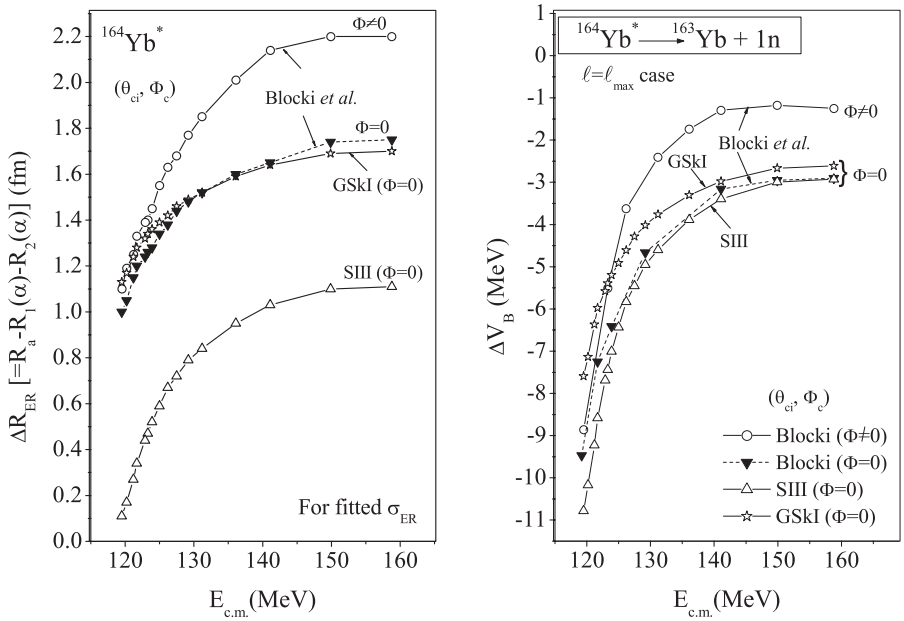

FIG. 6. (a) Variation of the neck-length parameter ΔR with $E_{\rm c.m.}$, obtained for the best fit to fusion-ER data in Fig. 5, using Blocki *et al.* interaction and Skyrme forces SIII and GSkI. For Blocki *et al.*, both the cases of coplanar ($\Phi = 0$) and non-coplanar ($\Phi \neq 0$) nuclei are considered. The ER is taken to consist of LPs $= xn, x = 1$–4. (b) Same as for (a) but the variation of the "barrier-lowering" parameter ΔV_B for $\ell = \ell_{\rm max}$, with $E_{\rm c.m.}$ for the case of $1n$ decay, defined by Eq. (5) and in Fig. 2.

from above-barrier to below-barrier energies. The interesting results are as follows. (i) Different nuclear interactions result in different functional dependencies for $\Delta R(T)$, but happen to be nearly identical for some forces [compare Blocki *et al.* ($\Phi_c = 0$ case) with GSkI, though the one for Blocki *et al.* is for $\theta_i^{\rm opt}$ [7] and GSkI for θ_{ci}]. This has important consequences for the choice of a proper nuclear interaction, which is shown more explicitly in Ref. [47] for the use of the extended-Wong model. (ii) In going from $\Phi_c = 0$ to $\Phi_c \neq 0$ for the Blocki *et al.* interaction, ΔR increases significantly, more so at higher $E_{\rm c.m.}$ (equivalently, T) values. The increase in ΔR means that the reaction time decreases, that is, the reaction becomes relatively more prompt, and that, by definition, the barrier-lowering parameter ΔV_B decreases. This is illustrated in Fig. 6(b) for $1n$ emission from ^{164}Yb* (the same result holds good for $2n$, $3n$, and $4n$ decays). Only the case of $\ell = \ell_{\rm max}$ is shown here, and exactly the same result is evident from Fig. 2 at other ℓ values. We notice in Fig. 6(b) that the variation of ΔV_B with $E_{\rm c.m.}$ is of similar order for all the three interactions for $\Phi = 0$ case (coplanar nuclei). For the non-coplanar ($\Phi \neq 0$) case, however, ΔV_B decreases considerably, more so at higher energies, which signifies a decrease in "fusion hindrance effect" owing to the addition of non-coplanar degree of freedom Φ. The hindrance effect is apparently more at sub-barrier energies, a built-in property of DCM [7].

Finally, it may be noted from Fig. 2 that in DCM, the ΔR and $\ell_{\rm max}$ are related quantities, and our choice of ΔR is good within $\ell_{\rm max} \pm 1$, fixed for LPs cross section $\sigma_{\rm ER} \to 0$ at $\ell = \ell_{\rm max}$ value. Figure 7 shows the variation of $\ell_{\rm max}(E_{\rm c.m.})$ for both coplanar and non-coplanar considerations. We notice that it is a smooth function both at below and above barrier energies for the Skyrme forces as well as Blocki *et al.* interaction. Evidently, in DCM, the physics of the problem is shown to be contained in ΔR or, equivalently, in $\ell_{\rm max}$ or ΔV_B as a function of $E_{\rm c.m.}$, introduced first in Ref. [7] for coplanar nuclei ($\Phi = 0$) and extended here to non-coplanar nuclei ($\Phi \neq 0$), including also the role of using different nuclear proximity potentials.

B. Fusion-fission cross sections: Role of non-coplanarity and different nuclear interactions on quasifission component and constituents of fusion-fission process

The calculated ff excitation function $\sigma_{\rm ff}^{\rm Cal.}(E_{\rm c.m.})$ is also given in Table I, and plotted in Fig. 8(a), for the $\Delta R(E_{\rm c.m.})$ fitted to CASCADE data [1], as shown in Fig. 8(b) for the Blocki

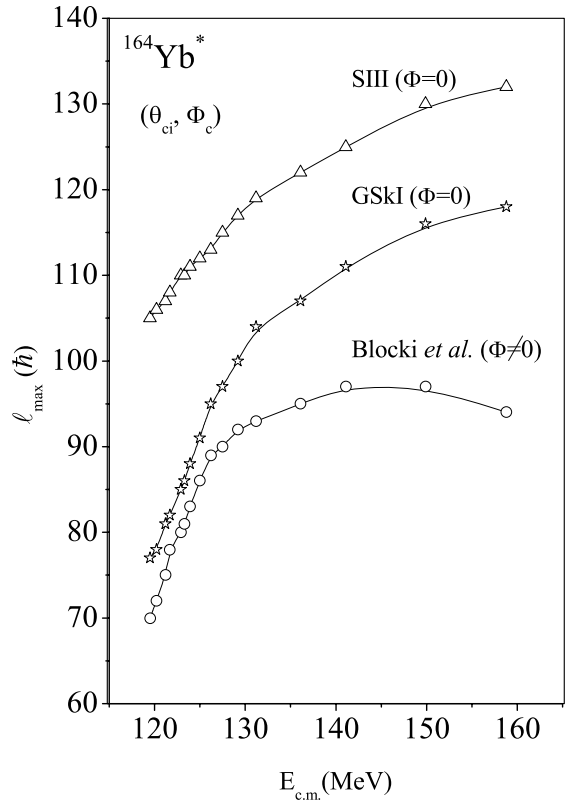

FIG. 7. Same as for Fig. 6(a), but for $\ell_{\rm max}$ as a function of $E_{\rm c.m.}$. For Blocki *et al.*, only the case of non-coplanar ($\Phi \neq 0$) nuclei is shown.

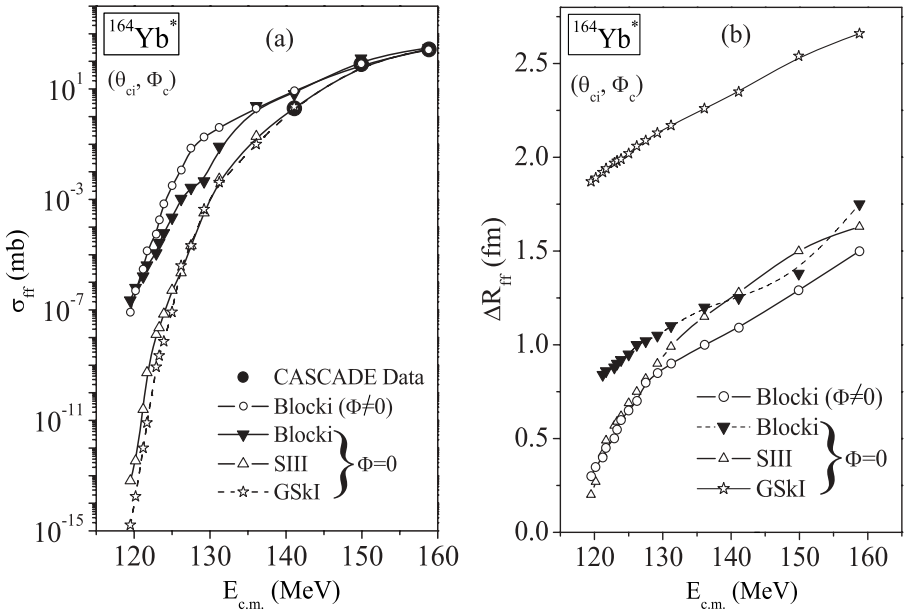

FIG. 8. (a) Same as for Fig. 5, but for the ff cross section $\sigma_{\rm ff}$. The DCM calculated $\sigma_{\rm ff}^{\rm Cal.}$ for different nuclear proximity interactions, for coplanar ($\Phi = 0$) and non-coplanar ($\Phi \neq 0$) cases is compared with CASCADE data from Ref. [1]. (b) The neck-length parameter ΔR as a function of $E_{\rm c.m.}$ for the simultaneously fitted ff cross section $\sigma_{\rm ff}^{\rm CASCADE}$.

et al. ($\Phi = 0$ and $\Phi \neq 0$) interaction and the two Skyrme forces ($\Phi = 0$). The $\Phi = 0$ case of Blocki *et al.* interaction is from Ref. [7]. For comparison, the CASCADE data are also given in Table I as well as in Fig. 8(a). We notice from Table I and Ref. [7] that the components of $\sigma_{\rm ff}^{\rm Cal.}$ are different for different cases of interaction and angle Φ (further shown in Fig. 9, and discussed below). We notice in Table I and Fig. 8(a) that the fits are nearly exact for both the Skyrme forces, but show some disagreement for at least the highest energy and hence the possible presence of some qf component in both the cases ($\Phi = 0$ or $\Phi \neq 0$) of Blocki *et al.* interaction. Note that, at near- and below-barrier energies, all calculations predict the $\sigma_{\rm ff}$ to be small or nearly zero, in agreement with CASCADE data. The $\Delta R_{\rm ff}$ in Fig. 8(b) show that they are different from $\Delta R_{\rm ER}$ obtained in Fig. 6(a) for $\sigma_{\rm ER}$, but are nearly the same for all cases except for the GSkI ($\Phi = 0$) force. For GSkI, $\Delta R_{\rm ff}$ is rather large, which happens because the barrier in this case lies at a much larger R value (see, e.g., Fig. 3 in Ref. [13] or Fig. 6 in Ref. [47]), and hence, compared to SIII force, the R_a is larger for GSkI force.

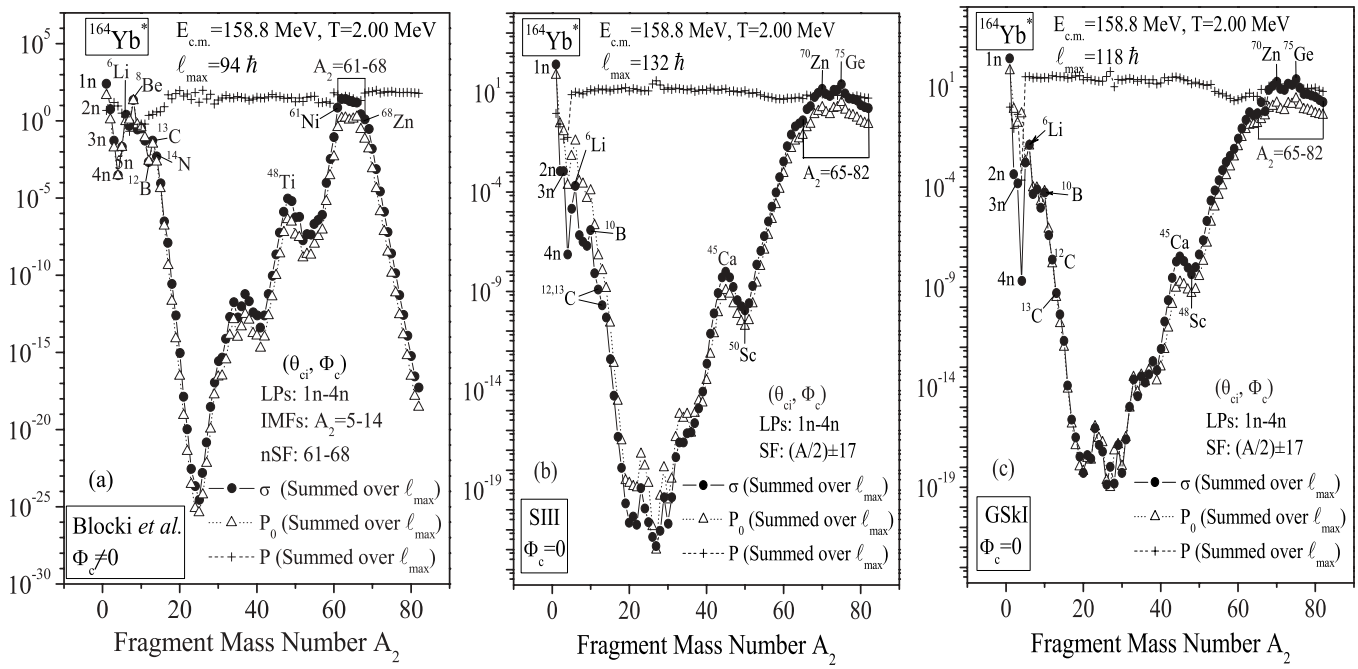

FIG. 9. The ℓ-summed fragment preformation probability P_0, penetrability P, and the decay cross section σ (in mb), as a function of the light fragment mass number A_2, for compound system ^{164}Yb* at $E_{\rm c.m.} = 158.8$ MeV for different interactions and both the $\Phi = 0$ and the $\Phi \neq 0$ cases.

Figure 9 depicts the ℓ-summed P_0, P, and σ as the function of the light-mass fragment A_2 for the highest-energy $E_{\rm c.m.} = 158.8$ MeV in ^{64}Ni + ^{100}Mo $\rightarrow$ ^{164}Yb* reaction, using the three nuclear interaction potentials for both the coplanar and the non-coplanar cases. Measurements of such decay cross sections as a function of CN excitation energy $E^*_{\rm CN}$, for some light fragments of the CN ^{164}Yb*, are available [51], but all at higher incident c.m. energies ($E_{\rm c.m.} > 195$ MeV). Hence, a direct comparison between the calculations and data is not possible. However, we first compare the case of $\Phi \neq 0$ for Blocki *et al.* interaction in Fig. 9(a) with its $\Phi = 0$ case in Fig. 10 of Ref. [7]). Interestingly, in going from $\Phi = 0$ to $\Phi \neq 0$, the components of $\sigma_{\rm ff}^{\rm Cal.}$ reduce from IMF + HMF + SF to only IMF + nSF. In particular, the peak around ^{45}Ca or ^{48}Ti, referring to the HMF region $A_2 = 40$–50 in the $\Phi = 0$ case, is now lowered, and the other peaks around ^{70}Zn and ^{75}Ge, referring to the SF region $A/2 \pm 20$ (for $\Phi = 0$ case), disappear, such that for the $\Phi \neq 0$ case, only IMF ($A_2 = 5$–14) and nSF ($A_2 = 61$–68) contribute to $\sigma_{\rm ff}$. However, in changing the interaction from Blocki *et al.* ($\Phi = 0$) to Skyrme forces ($\Phi = 0$), only the SF component $A/2 \pm 17$ or ± 20 contributes. In other words, both the non-coplanarity and choice of nuclear interactions are important for the predictions of various components of $\sigma_{\rm ff}$. In addition, the qf component is also possible, as noted in the last paragraph above. Thus, experimental measurements of $\sigma_{\rm ff}$ are called for.

IV. SUMMARY

Application of the DCM, made to ^{64}Ni + ^{100}Mo $\rightarrow$ ^{164}Yb* reaction with measured ER cross sections at both below- and above-barrier energies, for use of the Blocki *et al.* nuclear proximity potential to "optimally" oriented coplanar ($\Phi = 0$) nuclei, is extended here to include the deformations up to hexadecapole (β_4) and "compact" orientations of non-coplanar ($\Phi \neq 0$) nuclei, as well as to the use of various other nuclear proximity potentials derived from the semiclassical ETF approach in SEDF. The Skyrme forces SIII and GSkI are used, and the densities for CN are added in frozen-density approximation.

The fusion-evaporation cross section, consisting of x neutrons ($x = 1$–4), is fitted to the only parameter of the model, the neck-length parameter ΔR. For a best fit to the data, ΔR as a function of $E_{\rm c.m.}$ increases considerably in going from $\Phi = 0$ to $\Phi \neq 0$ case, and more so at higher c.m. energies. For the $\Phi = 0$ case, $\Delta R(E_{\rm c.m.})$ is different for the two Skyrme forces, and the GSkI (for compact orientations θ_{ci}) behaves similar to that of Blocki *et al.* (for optimum orientations $\theta_i^{\rm opt}$). Different values of ΔR for different interactions and Φ values have important consequences for the reaction times, as well as the "barrier-lowering" parameter responsible for fusion hindrance phenomenon. Apparently, as ΔR increases, both the reaction time and the barrier-lowering parameter ΔV_B decrease. Thus, fusion hindrance effect is different for different nuclear interactions, and with the inclusion of non-coplanar degree of freedom it decreases considerably, particularly at higher center-of-mass energies.

For the ff process, only the CASCADE data is available at the three highest above-barrier energies. At near- and below-barrier energies, the CASCADE analysis predicts zero ff cross section. For the simultaneous fitting of the neck-length parameter, we find that the components of fission cross section are different for different interaction potentials and for coplanar ($\Phi = 0$) and non-coplanar ($\Phi \neq 0$) nuclei. For $\Phi = 0$ case, the fit to data is almost exact for the two Skyrme forces, but show the necessity of qf component in the case of Blocki *et al.* interaction, which does not get reduced, even when including the case of non-coplanar ($\Phi \neq 0$) nuclei. The two Skyrme forces predict the SF with $A/2 \pm 17$ alone for the $\Phi = 0$ case, whereas in going from $\Phi = 0$ to $\Phi \neq 0$ configurations, the constituents of fission cross section for Blocki *et al.* interaction change from a sum of IMFs ($A_2 = 5$–20), HMFs ($A_2 = 40$–50), and the SF ($A/2 \pm 20$) to IMFs ($A_2 = 5$–14) and nSF ($A_2 = 61$–68) plus the complimentary heavier fragments. Only the availability of experimentally measured ff cross section would decide the role of non-coplanarity and the best operative nuclear interaction.

ACKNOWLEDGMENTS

Financial support of Council of Scientific and Industrial Research (CSIR) and Department of Science and Technology (DST), New Delhi is duly acknowledged. One of us (R.K.) is thankful to UGC for the financial support under the Dr. D. S. Kothari Post Doctoral Program.

[1] C. L. Jiang *et al.*, Phys. Rev. C **71**, 044613 (2005).
[2] D. Ackermann, B. B. Back, R. R. Betts, M. Carpenter, L. Corradi, S. M. Fischer, R. Ganz, S. Gil, G. Hackman, D. J. Hofman, R. V. F. Janssens, T. L. Khoo, G. Montagnoli, V. Nanal, F. Scarlassara, M. Schlapp, D. Seweryniak, A. M. Stefanini, and A. H. Wuosman, Nucl. Phys. A **630**, 442c (1998); J. Phy. G: Nucl. Part. Phys. **23**, 1167 (1997).
[3] M. L. Halbert, J. R. Beene, D. C. Hensley, K. Honkanen, T. M. Semkow, V. Abenante, D. G. Sarantites, and Z. Li, Phys. Rev. C **40**, 2558 (1989).
[4] S. Misicu and H. Esbensen, Phys. Rev. Lett. **96**, 112701 (2006); Phys. Rev. C **75**, 034606 (2007).
[5] R. Kumar, M. Bansal, S. K. Arun, and R. K. Gupta, Phys. Rev. C **80**, 034618 (2009).
[6] R. K. Gupta and M. Bansal, Int. Rev. Phys. (I. RE. PHY.) **5**, 74 (2011).
[7] S. K. Arun, R. Kumar, and R. K. Gupta, J. Phys. G: Nucl. Part. Phys. **36**, 085105 (2009).
[8] M. G. Itkis *et al.*, J. Nucl. Radiochem. Sciences **3**, 57 (2002).
[9] J. Blocki, J. Randrup, W. J. Swiatecki, and C. F. Tsang, Ann. Phys. (NY) **105**, 427 (1977).
[10] R. K. Gupta, M. Balasubramaniam, R. Kumar, N. Singh, M. Manhas, and W. Greiner, J. Phy. G: Nucl. Part. Phys. **31**, 631 (2005).

[11] R. K. Gupta, M. Manhas, and W. Greiner, Phys. Rev. C **73**, 054307 (2006).
[12] R. K. Gupta, D. Singh, R. Kumar, and W. Greiner, J. Phys. G: Nucl. Part. Phys. **36**, 075104 (2009).
[13] R. Kumar, M. K. Sharma, and R. K. Gupta, Nucl. Phys. A **870-871**, 42 (2011).
[14] P. Möller, J. R. Nix, W. D. Myers, and W. J. Swiatecki, At. Data Nucl. Data Tables **59**, 185 (1995).
[15] M. K. Sharma, G. Sawhney, R. K. Gupta, and W. Greiner, J Phys. G: Nucl. Part. Phys. **38**, 105101 (2011).
[16] R. K. Gupta, in *Clusters in Nuclei*, Lecture Notes in Physics 818, edited by C. Beck (Springer-Verlag, Berlin, Heidelberg, 2010), Vol. I, p. 223.
[17] R. Kumar and R. K. Gupta, Phys. Rev. C **79**, 034602 (2009).
[18] R. K. Gupta, S. K. Arun, R. Kumar and Niyti, Int. Rev. Phys. (I. RE. PHY.) **2**, 369 (2008).
[19] B. B. Singh, M. K. Sharma, and R. K. Gupta, Phys. Rev. C **77**, 054613 (2008).
[20] M. Muenchow and W. Scheid, Nucl. Phys. A **468**, 59 (1987).
[21] M. Rashdan, A. Faessler, and W. Waida, J. Phys. G: Nucl. Part. Phys. **17**, 1401 (1991).
[22] B. B. Singh, M. K. Sharma, R. K. Gupta, and W. Greiner, Int. J. Mod. Phys. E **15**, 699 (2006).
[23] S. J. Sanders, D. G. Kovar, B. B. Back, C. Beck, D. J. Henderson, R. V. F. Janssens, T. F. Wang, and B. D. Wilkins, Phys. Rev. C **40**, 2091 (1989).
[24] G. Royer and J. Mignen, J. Phys. G: Nucl. Part. Phys. **18**, 1781 (1992).
[25] S. Kumar and R. K. Gupta, Phys. Rev. C **55**, 218 (1997).
[26] H. S. Khosla, S. S. Malik, and R. K. Gupta, Nucl. Phys. A **513**, 115 (1990).
[27] R. K. Gupta, S. Kumar, and W. Scheid, Int. J. Mod. Phys. E **6**, 259 (1997).
[28] T. Matsuse, C. Beck, R. Nouicer, and D. Mahboub, Phys. Rev. C **55**, 1380 (1997).
[29] S. J. Sanders, Phys. Rev. C **44**, 2676 (1991).
[30] H. Kröger and W. Scheid, J. Phys. G **6**, L85 (1980).
[31] J. Maruhn and W. Greiner, Phys. Rev. Lett. **32**, 548 (1974).
[32] R. K. Gupta, W. Scheid, and W. Greiner, Phys. Rev. Lett. **35**, 353 (1975).
[33] R. Aroumougame, N. Malhotra, S. S. Malik, and R. K. Gupta, Phys. Rev. C **35**, 994 (1987).
[34] N. J. Davidson, S. S. Hsiao, J. Markram, H. G. Miller, and Y. Tzeng, Nucl. Phys. A **570**, 61c (1994).
[35] P. A. Seeger, Nucl. Phys. A **25**, 1 (1961).
[36] W. Myers and W. J. Swiatecki, Nucl. Phys. **81**, 1 (1966).
[37] A. S. Jensen and J. Damgaard, Nucl. Phys. A **203**, 578 (1973).
[38] R. K. Gupta, R. Kumar, N. K. Dhiman, M. Balasubramaniam, W. Scheid, and C. Beck, Phys. Rev. C **68**, 014610 (2003).
[39] M. Balasubramaniam, R. Kumar, R. K. Gupta, C. Beck, and W. Scheid, J. Phys. G: Nucl. Part. Phys. **29**, 2703 (2003).
[40] B. B. Singh, M. K. Sharma, R. Kumar, M. Bansal, and R. K. Gupta (to be published).
[41] R. A. Gherghescu, Phys. Rev. C **67**, 014309 (2003).
[42] R. K. Gupta, D. Singh, and W. Greiner, Phys. Rev. C **75**, 024603 (2007).
[43] S. Shlomo and J. B. Natowitz, Phys. Rev. C **44**, 2878 (1991).
[44] M. Brack, C. Guet, and H.-B. Hakansson, Phys. Rep. **123**, 275 (1985).
[45] J. Friedrich and P.-G. Reinhard, Phys. Rev. C **33**, 335 (1986).
[46] B. K. Agrawal, S. K. Dhiman, and R. Kumar, Phys. Rev. C **73**, 034319 (2006).
[47] D. Jain, R. Kumar, M. K. Sharma, and R. K. Gupta, Phys. Rev. C **85**, 024615 (2012).
[48] R. K. Gupta, N. Singh, and M. Manhas, Phy. Rev. C **70**, 034608 (2004).
[49] M. Manhas and R. K. Gupta, Phys. Rev. C **72**, 024606 (2005).
[50] R. K. Gupta, Phys. Rev. C **21**, 1278 (1980).
[51] R. J. Charity, M. Korolija, D. G. Sarantites, and L. G. Sobotka, Phys. Rev. C **56**, 873 (1997).